Role of ephaptic coupling in discordant alternans domain sizes and action potential propagation in the heart

Niels F. Otani,[1,*] Eileen Figueroa,[2] James Garrison,[3] Michelle Hewson,[4] Laura Muñoz,[1] Flavio H. Fenton,[5]
Alain Karma,[6] and Seth H. Weinberg[7]
[1]*School of Mathematical Sciences, Rochester Institute of Technology, Rochester, New York 14623, USA*
[2]*Department of Electrical, Computer and Telecommunications Engineering Technology, Rochester Institute of Technology, Rochester, New York 14623, USA*
[3]*Department of Mathematics and Computer Science, Hampden-Sydney College, Hampden-Sydney, Virginia 23943, USA*
[4]*Department of Mathematics and Computer Science, Western Carolina University, Cullowhee, North Carolina 28723, USA*
[5]*School of Physics, Georgia Institute of Technology, Atlanta, Georgia 30332, USA*
[6]*Physics Department and Center for Interdisciplinary Research on Complex Systems, Northeastern University, Boston, Massachusetts 02115, USA*
[7]*Department of Biomedical Engineering, The Ohio State University, Columbus, Ohio 43210, USA*

(Received 19 October 2022; accepted 10 March 2023; published 23 May 2023)

Discordant alternans, the spatially out-of-phase alternation of the durations of propagating action potentials in the heart, has been linked to the onset of fibrillation, a major cardiac rhythm disorder. The sizes of the regions, or domains, within which these alternations are synchronized are critical in this link. However, computer models employing standard gap junction-based coupling between cells have been unable to reproduce simultaneously the small domain sizes and rapid action potential propagation speeds seen in experiments. Here we use computational methods to show that rapid wave speeds and small domain sizes are possible when a more detailed model of intercellular coupling that accounts for so-called ephaptic effects is used. We provide evidence that the smaller domain sizes are possible, because different coupling strengths can exist on the wavefronts, for which both ephaptic and gap-junction coupling are involved, in contrast to the wavebacks, where only gap-junction coupling plays an active role. The differences in coupling strength are due to the high density of fast-inward (sodium) channels known to localize on the ends of cardiac cells, which are only active (and thus engage ephaptic coupling) during wavefront propagation. Thus, our results suggest that this distribution of fast-inward channels, as well as other factors responsible for the critical involvement of ephaptic coupling in wave propagation, including intercellular cleft spacing, play important roles in increasing the vulnerability of the heart to life-threatening tachyarrhythmias. Our results, combined with the absence of short-wavelength discordant alternans domains in standard gap-junction-dominated coupling models, also provide evidence that both gap-junction and ephaptic coupling are critical in wavefront propagation and waveback dynamics.

DOI: 10.1103/PhysRevE.107.054407

I. INTRODUCTION

Ventricular fibrillation is a dangerous and lethal rhythm disorder of the heart. A spatiotemporal phenomenon called discordant alternans, first experimentally observed [1] and then described theoretically [2,3], may be an important cause of this disorder [4–6]. Electrical alternans is a complex emerging temporal pattern of electrical waves in the heart whose morphology alternates from one beat to the next, due to a period-doubling bifurcation at the cell level, generally arising during fast heart rates or short basic cycle lengths (BCLs) [7,8]. In discordant alternans, this temporal pattern develops spatially into regions that are out of phase with one another, with one or more regions exhibiting a long-short-long action potential duration (APD) pattern, while adjacent regions exhibit a short-long-short APD pattern [1]. As a result, large APD gradients can form in space, which provides a substrate susceptible to the formation of cardiac arrhythmias. However, the relationship between discordant alternans and arrhythmias has proven difficult to study computationally, because computer models of discordant alternans using the standard cable equation tend to yield out-of-phase regions, or domains, too large to fit within the heart (i.e., several centimeters in size), in particular in the presence of physiologically realistic conduction velocities [2,9–13], whereas in experiment domains have been shown to occur with much smaller sizes (i.e., on the order of 1 cm or smaller) [6,13–19] even when conduction velocities are over 150 cm/s [20]. A recent experimental-computational study from one of us highlighted this apparent inconsistency [17].

Another discrepancy, which we hypothesize is related to differences in experimental and simulated discordant alternans domain sizes (as described below), is the value of gap-junction resistance. Experimental measurements have found a wide range of values for the gap-junction resistance, typically in the tens to hundreds of megaohms (a few to low hundreds of nanosiemens) [21–32], yet common values

---

[*] nfosma@rit.edu

for resistances used in simulations employing physical units are one to two orders of magnitude lower [33–39]. Many simulation studies represent cardiac tissue as a continuous spatial domain via the cable equation and thus do not specifically define discrete cells and the associated gap-junction resistances in physical units, but rather define cell-cell coupling through use of a diffusion coefficient D. However, a comparison of coupling term coefficients in the discretized reaction-diffusion partial differential equation ($D/\Delta x^2$) and the discrete cell representation ($1/(R_g C_t)$) also suggests that the diffusion coefficients typically used (on the order of $0.001\ \mathrm{cm}^2/\mathrm{ms}$) correspond to gap-junction resistances lower than experimental measurements. Here Δx is the spatial discretization, which is typically (though not always) the length of a cell, R_g is the gap-junction resistance, and C_t is the total membrane capacitance. (Note that both coefficients have units of inverse time and thus define time constants associated with the strength of the gap-junction-mediated cell-cell coupling.)

In both cases, the lower gap-junction resistance or higher diffusion coefficient values are generally chosen in simulations to match experimental observations of the action potential wave speed, which is typically at least in the 50–60 cm/s range. However, these same values also result in smaller APD gradients in simulations [40] and thus larger spatial domains during discordant alternans [2,9–13]. That is, simulations using resistances or diffusion coefficient values which allow realistic wave propagation speeds are generally unable to produce discordant alternans domains of realistic size. Thus, the two discrepancies appear to be related. This is the fundamental paradox we address in this study: How can both fast conduction velocity and the steep repolarization gradients apparently necessary for small domains be maintained in the same tissue?

We highlight that these inconsistencies are not just problematic for our ability to model wave propagation in the heart; further, they reflect fundamental inconsistencies with our current understanding of the interaction between cell-cell coupling, wave propagation, and alternans pattern formation. In a companion paper (Ref. [41]), we provide a plausible explanation for these discrepancies. In this paper, we describe these ideas in greater detail, and also explore additional properties of the mechanisms involved. We posit that the paradox is resolved by accounting for an additional cell-cell coupling mechanism, so-called ephaptic coupling, as previously described by several previous studies [33,42–54]. In brief, ephaptic coupling occurs due to the high density of sodium channels clustered at the cell-cell junctions and the narrow intercellular cleft space between cells. During wavefront propagation, activation of sodium channels in an upstream or prejunctional cell produces a fast-inward current that hyperpolarizes the narrow cleft space between coupled cells. This in turn increases the transmembrane potential of the downstream or postjunctional cell. For sufficient cleft hyperpolarization, this can activate sodium channels on the downstream cell. This coupling mechanism occurs in parallel with current directly passing between cells through gap junctions.

Many prior studies, including our own, have demonstrated that this ephaptic-coupling mechanism strongly influences cardiac conduction, thus tying the latter to tissue structural properties such as the width of the intercellular cleft space and the fraction of sodium channels near the cleft, in addition to the gap-junction resistance [33,43,47,51,54,55]. Indeed, even if the intercellular gap-junction resistance is much higher than the value commonly used in simulations, near-normal action potential wave propagation speeds are still possible through ephaptic coupling, as has been demonstrated by Kucera *et al.* [33].

In contrast, on the trailing edge of the action potential, the sodium channels are inactive under normal conditions, so ephaptic coupling is also absent and coupling between cells is mediated solely by conventional gap-junction resistance. Thus, the dynamics of the propagating action potential can be different on the leading and trailing edges of the wave. We note that no prior studies have addressed how the interaction between ephaptic and gap-junction coupling can impact spatial gradients that arise during the rapid rates that produce alternans.

This "decoupling" between the mechanisms involved in wavefront and waveback dynamics allows us to advance the following hypothesis: Tissue characterized by high gap-junction resistance (tens to hundreds of megaohms) and strong ephaptic effects, as created by a combination of optimal cleft spacing and a high density of sodium channels on the ends of cells, admits the possibility of the simultaneous presence of rapidly propagating action potential waves and small discordant alternans domain sizes. Specifically, both strong ephaptic effects and gap junctions participate during the wavefront to permit rapid wave propagation while at the same time the high gap-junction resistivity reduces cell-cell coupling on the waveback, allowing steep APD spatial gradients, which facilitates the development of small discordant alternans domain sizes.

II. METHODS

To test our hypothesis, we constructed a computer model of a one-dimensional fiber, which employs a simplified version of the circuit previously used by Kucera *et al.* [33] and us [43,52,56] to model gap-junction and ephaptic-coupling effects. As shown in Fig. 1, the intracellular space of each cell is discretized into three nodes such that the intracellular resistance is modeled by two resistors R_i in each cell. The cleft region between cells is represented by one node, to which all the ephaptic-related components (shown in red in Fig. 1) are connected.

To define the passive components in this circuit, we followed the geometrically based procedure described by Kucera *et al.* Accordingly, we first chose both the intracellular and cleft resistivities ρ_i and ρ_{cl}, respectively, to be $150\ \Omega\,\mathrm{cm}$ and the capacitance per unit membrane surface area c_m to be $1.0\ \mu\mathrm{F/cm}^2$. The values of the resistances $R_i = \rho_i \Delta x/(2\pi r^2)$ and $R_r = \rho_{\mathrm{cl}}/(8\pi w_{\mathrm{cl}})$ and capacitances $C_m = c_m A_m$ and $C_{\mathrm{cl}} = c_m A_{\mathrm{cl}}$ were then calculated assuming a cylindrical cell shape of length $\Delta x = 100\ \mu\mathrm{m}$ and radius $r = 11\ \mu\mathrm{m}$, where $A_{\mathrm{cl}} = \pi r^2$ and $A_m = 2\pi r \Delta x$ are the areas of the end and lateral surface of each cell, respectively, with cells arranged end-to-end to form the fiber, and assuming the cleft region is a disk-shaped region between each pair of cells, with the same radius as the cells and width w_{cl}, which varied in our simulations from 2 to 60 nm [50,55]. The value of gap-junction resistance R_g was varied from $3.95\ \mathrm{M}\Omega$ to $395\ \mathrm{M}\Omega$ (equiva-

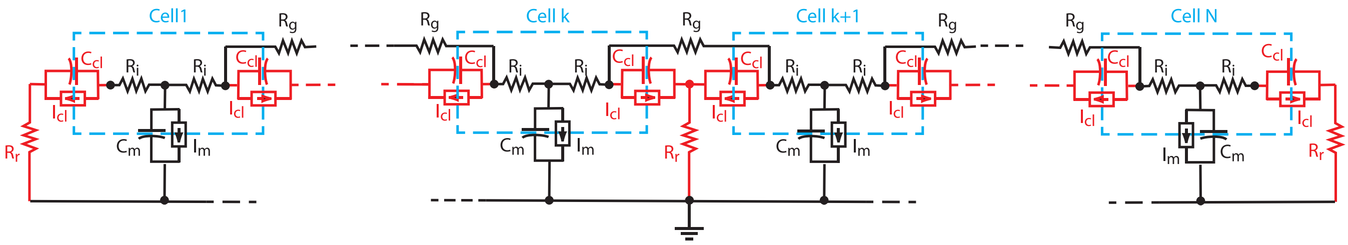

FIG. 1. Circuit used to model a one-dimensional fiber containing gap-junction and ephaptic intercellular coupling. Black circuit elements are those typically used in standard monodomain models of one-dimensional fibers. Red elements model ephaptic coupling. Blue dashed boxes indicate the locations of cells within this circuit description of the fiber.

lently, the gap-junction conductance varied from 253 nS down to 2.53 nS).

The remaining components appearing in the circuit, I_m and $I_{\rm cl}$, were then defined using a modified version of the three-variable Echebarria-Karma ionic model [57]. Here I_m and $I_{\rm cl}$ are the ionic currents flowing across the membrane at the lateral and cleft surfaces, respectively, as depicted in Fig. 1. Importantly, this minimal model is well established in the investigation of cellular and tissue-scale alternans dynamics [58,59]. In the model, the transmembrane voltage dynamics are described in terms of a normalized unitless voltage $u = (V - V_{\rm rest})/(V_{\rm act} - V_{\rm rest})$, where $V_{\rm act} = 15$ mV and $V_{\rm rest} = -85$ mV are the fully activated and resting-state membrane potentials, respectively, and normalized current, with units of inverse time,

$$J_{\rm fi}^s = \sigma_{\rm fi}^s h m_\infty(u)(u - 1.3)/\tau_{\rm fi}, \tag{1}$$

$$J_{\rm si}^s = f d_\infty(u)(u - 1.4)/\tau_{\rm si}, \tag{2}$$

$$J_{\rm so}^s = [1 - \exp(-4u)]/\tau_{\rm so}, \tag{3}$$

where normalized fast-inward ($J_{\rm fi}^s$), slow-inward ($J_{\rm si}^s$), and slow-outward ($J_{\rm so}^s$) currents broadly correspond to sodium, calcium, and potassium currents, respectively. Here the superscript s ($s = {\rm cl}$ or m) denotes currents on either the cleft or lateral membrane surface, respectively (as shown in Fig. 1). The parameter $\sigma_{\rm fi}^s$ is used to vary the relative surface densities of the fast-inward current between these two membrane surfaces (additional details below). The sum of these ionic currents (in units of μA) is then given by

$$I_s = \left(J_{\rm fi}^s + J_{\rm si}^s + J_{\rm so}^s\right) c_m (V_{\rm act} - V_{\rm rest}) A_s. \tag{4}$$

Evolution of the gating variables, fast-inward inactivation gate h, and slow-inward inactivation gate f for each membrane current were governed by the rate equations

$$dh/dt = [h_\infty(u) - h]/\tau_h(u), \tag{5}$$

$$df/dt = [f_\infty(u) - f]/\tau_f(u). \tag{6}$$

The steady-steady fast-inward activation m_∞, fast-inward inactivation h_∞, slow-inward activation d_∞, and slow-inward inactivation f_∞ functions were defined piecewise such that, for $u \geqslant 0$,

$$m_\infty(u) = (u/0.2)^p/[1 + (u/0.2)^p], \tag{7}$$

$$h_\infty(u) = 1/[1 + (u/0.1)^6], \tag{8}$$

$$d_\infty(u) = (u/0.4)^4/[1 + (u/0.4)^4], \tag{9}$$

$$f_\infty(u) = 1/[1 + (u/0.1)^4], \tag{10}$$

while for $u < 0$ we defined $m_\infty(u) = 0$, $h_\infty(u) = 1$, $d_\infty(u) = 0$, and $f_\infty(u) = 1$, respectively. The voltage-dependent time constants were given by

$$\tau_h(u) = \tau_{h_1} + \tau_{h_2} \exp[-20(u - 0.1)^2], \tag{11}$$

$$\tau_f(u) = \tau_{f_2} + \left(\tau_{f_1} - \tau_{f_2}\right)u^3. \tag{12}$$

We note that in this model with normalized currents, the inverse of the current time constants ($\tau_{\rm fi}$, $\tau_{\rm si}$, and $\tau_{\rm so}$) correspond to current conductances. To increase the maximum possible APD to values typically seen in discordant alternans experiments (around 200 ms in canines), we increased all the timescale parameters appearing in [57] that are involved in determining the APD by a factor of 1.5 such that $\tau_{\rm so} = 1.5{\times}15.0$, $\tau_{\rm si} = 1.5{\times}4.1$, $\tau_{h1} = 1.5{\times}4.8$, $\tau_{f1} = 1.5{\times}100$, $\tau_{f2} = 1.5{\times}30$, and $\tau_{h2} = 1.5{\times}6$ (in units of milliseconds). For similar reasons of matching action potential wave velocity [also known as the conduction velocity (CV)] to 50–60 cm/s, we increased the fast-inward current conductance by increasing the inverse of the fast-inward (sodium) time constant $\tau_{\rm fi}^{-1}$ to values between 3.0 and 5.0 ms^{-1} (from a baseline value of 1.25 ms^{-1}). This larger fast-inward current triggered automaticity under some circumstances, so we increased the value of p from 6 to 8. This had the effect of decreasing the subthreshold fast-inward current, suppressing automaticity, while increasing the current above the threshold, thus leaving the CV roughly unchanged.

To compare the patterns of classical action potential (AP) wave propagation, which is principally mediated by gap-junction coupling, to AP propagation mediated by both ephaptic and gap-junction coupling, we included two new parameters $\sigma_{\rm fi}^{\rm cl}$ and $\sigma_{\rm fi}^m$ in Eq. (1), which allowed us to modify the surface density of fast-inward (sodium) channels on cleft-facing membranes relative to the corresponding density on lateral membranes. To study gap-junction-dominated wave propagation, we simply set $\sigma_{\rm fi}^{\rm cl} = \sigma_{\rm fi}^m = 1$ (i.e., uniform distribution of fast-inward channels). In contrast, ephaptic-coupling-mediated wave propagation requires a high density of sodium channels on the ends compared to the lateral surface, which has been demonstrated by several myocyte microscopy studies [55,60–62]. Accordingly, to study ephaptic-mediated propagation, we modified the fast-inward currents by defining $\sigma_{\rm fi}^{\rm cl}$ to be much larger than $\sigma_{\rm fi}^m$ (described further below). Note that for all cases we assumed a uniform distribution for both slow-inward and slow-outward currents, based on recent evidence of potassium [63–66] and calcium

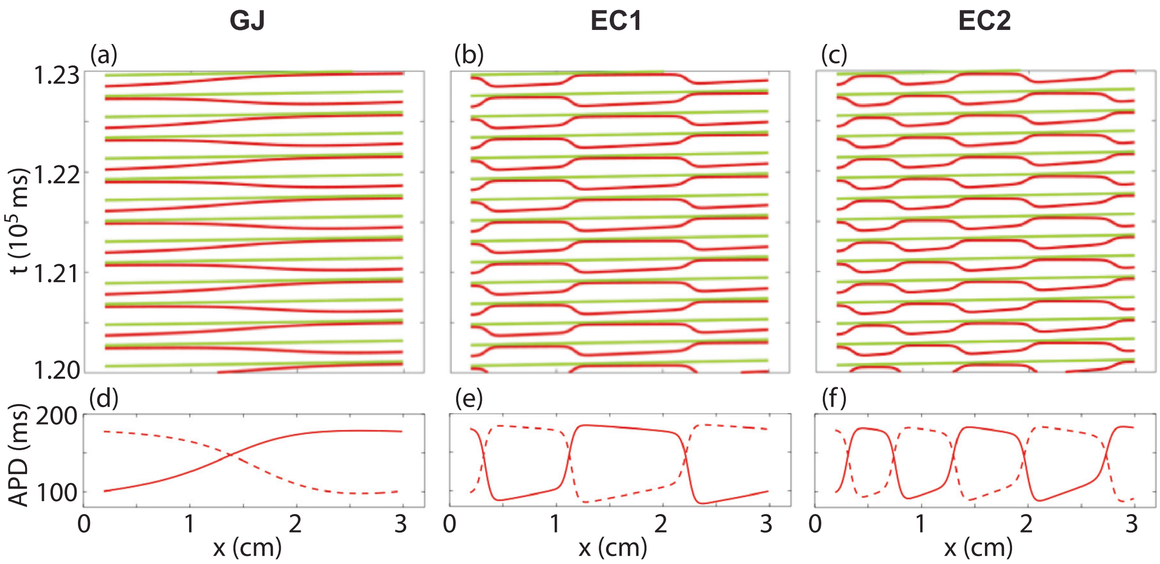

FIG. 2. Wavefront and waveback arrival times (nearly straight green and distinctly curved red traces, respectively) vs arrival location x along the fiber for (a) the GJ system, (b) the EC1 system, and (c) the EC2 system. Waves were launched from the left end of the system at regular intervals. The pacing interval was 207 ms. Data are shown approximately 120 s into the simulations, well after initial transient behavior has dissipated. (d)–(f) APD(x) vs x for the last two complete waves shown in (a)–(c) (the last wave is shown by the solid trace and the penultimate wave by the dashed trace). The wavefront and waveback arrival times were defined to be the times the membrane potential V ascended or descended to the level of −65 mV, respectively. The APD was defined to be the difference between these two times.

[67] channels also being present at the cell ends, in addition to lateral membranes.

To advance the circuit equations from one time step to the next, we solved the equations obtained by applying Kirchhoff's current law to each node in the electric circuit. In solving these equations, we evaluated the currents flowing through the resistors at the future time step (i.e., backward Euler), while currents through the nonlinear ion channel currents I_m and $I_{\rm cl}$ were evaluated at the present time step (forward Euler). This allowed us to use a time step of 0.01 ms while still maintaining numerical stability. This time step was still small enough to accurately advance the nonlinear ion channel currents. Additional details of the circuit time-stepping algorithm appear in Appendix A. The gating variables h and f were also advanced using the standard forward Euler method. Time steps both an order of magnitude larger and smaller were tried to ensure that the time step of 0.01 ms was sufficient to model, in particular, the action potential wave velocity, with reasonable accuracy. The system consisted of 320 cells, yielding a system length L of 3.2 cm. The MATLAB programming language (Mathworks, Inc.) was used for all computations.

III. RESULTS

We first demonstrated that our model produces the same long length scale pattern of discordant alternans others have seen for conditions for which wave propagation is mediated by standard gap-junction coupling [2,9–13]. With uniform fast-inward ionic current density (i.e., $\sigma_{\rm fi}^m = \sigma_{\rm fi}^{\rm cl} = 1$), a relatively low gap-junction resistance $R_g = 3.95$ MΩ, a fast-inward conductance $\tau_{\rm fi}^{-1}$ of 3.0 ms^{-1}, and a cleft width $w_{\rm cl}$ of 26 nm, we obtained a maximum wave velocity of 56.7 cm/s (i.e., in the limit of infinite previous diastolic interval). We refer to this system as the GJ system, to reflect the fact that conduction in this case is primarily mediated by gap-junction coupling. When waves were launched from the left end of the fiber (at $x = 0$ cm), at regular intervals of 207 ms, a classic discordant alternans pattern quickly developed, as illustrated by the pattern of the wavefronts (green) and wavebacks (red) in Fig. 2(a). By time $t = 120$ s, we found that, apart from an overall slow drift towards the pacing end of the system ($x = 0$), a discordant alternans pattern was established. Portions of two discordant alternans domains [i.e., regions in which the long-short-long-short patterns of APDs or diastolic intervals (DIs) are in phase] are evident, separated by a gradual transition region close to 1.0 cm wide, as shown in Fig. 2(d).

Next we considered the regime characterized by wave propagation that is mediated by ephaptic coupling, with gap-junction coupling playing a secondary role. Many prior studies have shown that a high cleft-localized surface density of fast-inward current is required for ephaptic coupling [33,43,48,51]. We implemented this condition by redistributing most (90%) of the fast-inward channels to the ends of the cells by setting $\sigma_{\rm fi}^{\rm cl} = 0.9(r + \Delta x)/r$ and $\sigma_{\rm fi}^m = 0.1(r + \Delta x)/\Delta x$, with this distribution estimated from patch clamp current recordings from the cell middle and ends [68]. This kept the total number of fast-inward channels unchanged while effectively increasing the ratio of the surface density of these ion channels on the cell ends to the density on the lateral surface from 1.0 to 81.0. To maintain a comparable conduction velocity in the presence of ephaptic coupling, we increased the gap-junction resistances 100-fold (to $R_g = 395.0$ MΩ), which is more comparable to values observed in experiment [21–32].

To verify that we were indeed in the ephaptic-coupling-mediated wave propagation regime, we ran several simulations in which a single wave was launched at $t = 0$ and $x = 0$

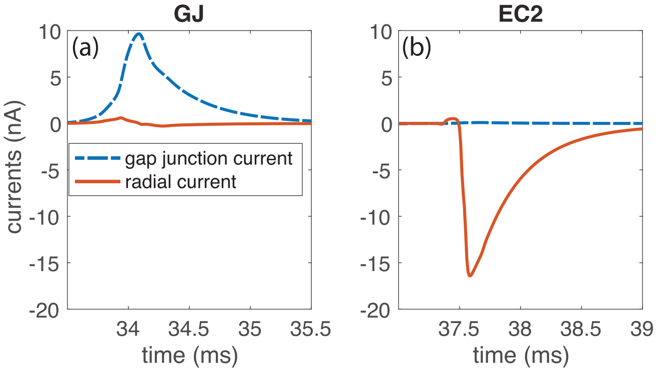

FIG. 3. Currents flowing through the gap-junction resistor R_g from left to right in Fig. 1 (blue dashed line) and through the radial resistor R_r to the ground (red solid line) in between cells 194 and 195 during wavefront propagation, in (a) the GJ system and (b) the EC2 system.

with initially no refractoriness present anywhere on the fiber ($h = f = 1.0$ at $t = 0$ in all cells). Figure 3 shows the currents flowing through the gap-junction and radial resistors R_g and R_r, at a point far from either end of the fiber, as the wave passed through this point (i.e., during the wavefront). Two representative cases are shown. For the GJ system described above, we see in Fig. 3(a) that the current through the gap junction dominates, illustrating that wavefront propagation is mediated by gap-junction coupling via the resistor R_g in this system. In contrast, for a case with prominent ephaptic coupling, in which most of the fast-inward channels are relocated to the ends of the cells and R_g is increased 100-fold, as described above, we see in Fig. 3(b) that the gap-junction current is very small while the current through R_r is large. (The specific system used here was the EC2 system, which is defined below.) This is consistent with the description of ephaptic-coupled wave propagation from Kucera *et al.*, in which firing of the cell on the upstream or prejunctional side of the cleft region creates a substantial voltage drop across the R_r resistor which hyperpolarizes the cleft space, promoting the firing of the downstream cell through activation of the downstream or postjunctional fast-inward current. In this case, the radial current shown in Fig. 3(b) created a negative potential in the cleft of −38 mV through Ohm's law. Since the downstream cell was still at the resting potential of −85 mV, the downstream fast-inward channels were raised to a potential of −47 mV, which was above the firing threshold.

We also examined these two currents on the wavebacks of the propagating waves (not shown). We found that the radial currents were negligible in both systems (less than 10^{-4} nA in absolute value in both). In contrast, the gap-junction current was non-negligible in both systems and approximately 100 times larger in the GJ system compared with EC2, consistent with the 100-times-smaller value of R_g. Thus, intercell coupling on the waveback is mediated primarily by gap junctions in both systems.

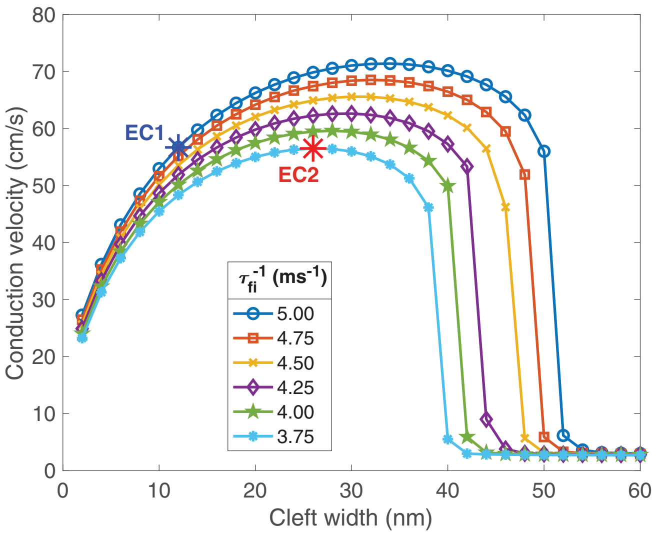

FIG. 4. Action potential wave velocities vs cleft width w_{cl} for different strengths of the fast-inward current, as characterized by τ_{fi}^{-1} (3.75 ms^{-1}, weakest, and 5.00 ms^{-1} strongest), for the case of $R_g =$ 395 MΩ and 90% of fast-inward current channels localized on the ends of the cells.

We note that the arrival times shown in Fig. 3 are comparable, being approximately 34 ms and approximately 37.5 ms for the GJ and EC2 systems, respectively, indicating that the wave velocities in the two systems are commensurate. To assess how wave velocities depended on key parameters for ephaptic coupling, we calculated velocities for cleft widths w_{cl} varying from 2 to 60 nm for several values of the fast-inward channel conductivity τ_{fi}^{-1} (Fig. 4). We found a substantial bump (or inverted U shape) in velocity as a function of w_{cl} for all values of τ_{fi}^{-1} (Fig. 4), again consistent with ephaptic-coupled wave propagation, as first described by Kucera *et al.* [33]. For a wide cleft width w_{cl}, the voltage drops across the R_r resistors were insufficient to promote firing of the downstream cell and thus wave propagation was mediated solely by gap junctions and was thus much slower. As the cleft width decreased, the mechanism of earlier activation of the fast-inward current on the downstream cell, termed self-activation [33,54], was engaged, resulting in faster wave velocity (the right side of the bump. For very narrow w_{cl}, the cleft hyperpolarization became so substantial that the fast-inward current driving force was reduced, which reduced the overall fast-inward current and thus slowed wave velocity, a phenomenon termed self-attenuation [33] (the left side of the bump). The peak of the curves occurred for a cleft width for which self-activation and self-attenuation were balanced in such a manner as to promote the fastest wave propagation. We note that the conduction velocities observed in the bump region (50–70 cm/s) are comparable to those in the GJ system.

We next ran long (150 s) simulations for several of the cases in the bump region, for w_{cl} between 12 and 26 nm and τ_{fi}^{-1} between 3.75 and 5.00 ms^{-1}. We found two distinct types of behavior. Two systems, which we will call EC1 and EC2, were chosen to illustrate these two behavior types. The locations of these two systems in parameter space are shown as asterisks in Fig. 4. These two systems were selected because they had restitution functions that are very similar to those of the GJ system; thus differences should be primarily due to the differences in the intercell coupling mechanism. A

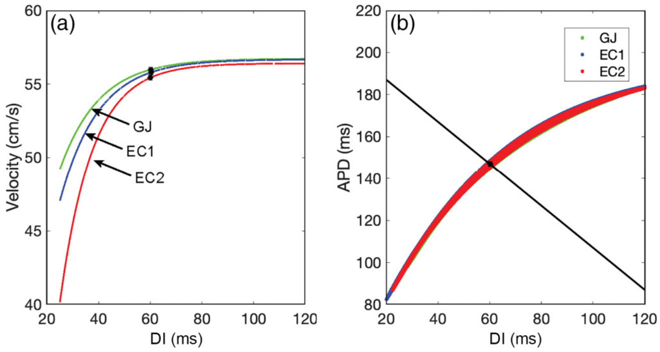

FIG. 5. (a) Conduction velocity and (b) APD restitution functions for the three systems, GJ (green line), EC1 (blue line), and EC2 (red line), for a cycle length (BCL) of 207 ms. Nonlinear regression was performed to construct the curves shown in both panels, assuming functions of the form $f(\mathrm{DI}) = \beta_1 - \beta_2 \exp(-\mathrm{DI}/\beta_3)$ in both cases. Additionally, scatterplot data from the three simulations are shown in (b). Data for the GJ and EC1 simulations are hidden underneath the EC2 data. The black dots show the location of the steady-state points in each plot: (a) $(\overline{\mathrm{DI}}, \overline{\mathrm{CV}})$ and (b) $(\overline{\mathrm{DI}}, \overline{\mathrm{APD}})$. The line $\overline{\mathrm{APD}} = \mathrm{BCL} - \overline{\mathrm{DI}}$ is also shown in (b).

comparison of the restitution functions of these three systems is shown in Fig. 5. In Fig. 5(a) we see that the three systems have similar maximum velocities of 55–57 cm/s. The EC1 and EC2 systems have velocity restitution functions that are slightly steeper than the GJ system, for short DIs. The APD restitution functions for all three systems are virtually identical [Fig. 5(b)]. Additionally, alternans formation in all three systems exhibited a nearly identical rate dependence: 1:1 behavior when paced at intervals above 215 ms, 2:2 behavior in the form of discordant alternans for pacing intervals between 199 and 215 ms, and 2:1 behavior (i.e., every other pacing stimulus fails to generate a wave) for pacing intervals below 199 ms.

Although these three systems had very similar velocity and APD restitution functions and rate dependence for the formation of alternans, the characteristics of discordant alternans spatial patterns, when they developed, were quite different. For the EC1 system (with parameters $\tau_{\mathrm{fi}}^{-1} = 5.00\ \mathrm{ms}^{-1}$ and $w_{\mathrm{cl}} = 12$ nm), three small-amplitude discordant alternans domains formed once the pacing interval fell below 216 ms. The amplitude grew rapidly as the pacing interval was shortened. Also, nodes in the discordant alternans pattern, that is, the boundary between domains, sharpened rapidly with decreasing pacing interval. The pattern of wavefront and waveback arrival times for a pacing cycle length of 207 ms is shown in Fig. 2(b). This pattern gave rise to an APD alternans amplitude pattern that was a nearly constant amplitude over most of the extent of each domain, as shown in Fig. 2(e), with transitions between domains occurring over comparatively short distances (i.e., the nodal width was relatively narrow compared to the GJ system). Additionally, as the pacing cycle length was decreased, the number of domains present on the fiber moderately increased, while the domain size moderately decreased, with almost five domains at a cycle length of 201 ms [Figs. 6(a) and 6(b), blue trace].

In the EC2 system ($\tau_{\mathrm{fi}}^{-1} = 3.75\ \mathrm{ms}^{-1}$ and $w_{\mathrm{cl}} = 26$ nm), discordant alternans again appeared, starting at a cycle length of 215 ms, with four domains present and steep transitions

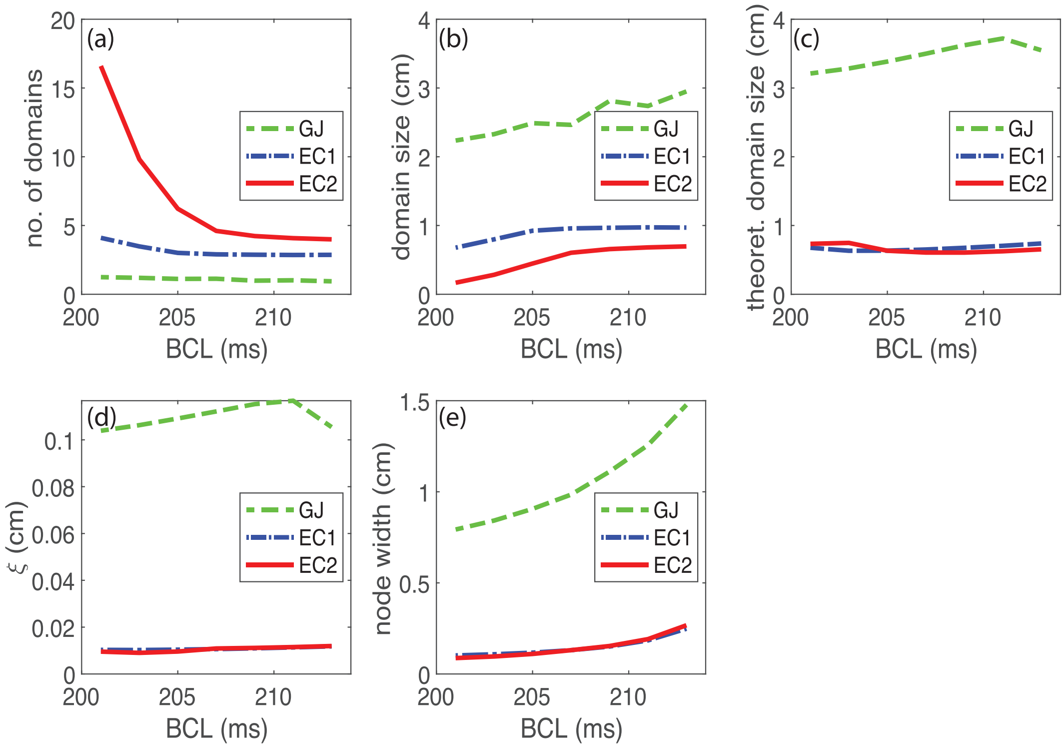

FIG. 6. Key discordant alternans domain parameters vs pacing cycle length. A description of the calculations of (a) the number of domains N_{domains}, (b) the domain size l_{domain}, (d) the APD coupling length ξ, and (e) the node width l_{node} is provided in Appendix B. The theoretical domain size in (c) is calculated from the formula $(2\pi/\sqrt{3})(2\xi^2\Lambda)^{1/3}$ (see the text).

soon developing in the space between domains. Figures 2(c) and 2(f) show these features for a pacing cycle length of 207 ms. Thus, both systems incorporating ephaptic coupling present with a larger number of smaller alternans domains and much smaller node widths compared to the GJ system. For both the EC1 and EC2 systems, smaller domains were also associated with larger voltage spatial gradients during repolarization. For the GJ system, the maximum $|dV/dx|$, calculated during repolarization, was 134 mV/cm, while for the EC1 and EC2 systems, this maximum gradient was 1429 and 1413 mV/cm, respectively.

However, in contrast with the EC1 system, which exhibited a modest dependence of the various domain properties on cycle length, in the EC2 system, the number of domains increased quite dramatically as the cycle length was decreased, with over 16 domains present for a pacing cycle length of 201 ms [cf. Fig. 6(a), red EC2 trace], with a corresponding decrease of the domain size down to about 0.1 cm, as shown in Fig. 6(b).

Importantly, the domain sizes in both the EC1 and EC2 systems were quite small (comparable to or much smaller than 1.0 cm), in sharp contrast to the GJ system, whose domain sizes were in the range of 2–3 cm in length for all cycle lengths, as shown in Fig. 6(b). These cases also show that, for ephaptic-coupling-mediated waves, the APD can vary quite sharply over short distances, allowing steep boundaries to exist between discordant alternans domains [compare, for example, Figs. 2(e) and 2(f) to Fig. 2(d)], which in turn facilitates the development of potentially many more domains of much smaller width in a tissue of given size.

It is worth mentioning that, while large transients associated with initial conditions (e.g., very long or short APDs and DIs) dissipate very rapidly, within the first second, certain subtler features evolve over a much longer period of time. Specifically, throughout the simulations, discordant alternans nodes were observed to enter slowly from the distal end of the system ($x = 3.2$ cm), travel across the system, and exit at the proximal end ($x = 0$). Even after $t = 150$ ms, the rates of entrance and exit of these nodes were not quite the same; this equilibration takes place over a much longer period of time. Since this process occurs over a much longer timescale, we do not believe it affects the conclusions of this study.

We next describe several additional length scales of the GJ, EC1, and EC2 regimes, which specifically highlight how incorporation of ephaptic coupling can support short spatial scale length changes in APD. First, we used nonlinear multiple regression to calculate two characteristic length scales w (not to be confused with w_{cl}) and ξ, defined from the assumed relationship

$$\text{APD}(x) = a(\text{DI}(x)) - w\frac{d}{dx}a(\text{DI}(x)) + \xi^2\frac{d^2}{dx^2}a(\text{DI}(x)), \tag{13}$$

where $a(\text{DI})$ is the APD restitution function we obtain when the preceding DI is independent of x [e.g., Fig. 5(b)]. As originally described by Echebarria and Karma [69], ξ represents the characteristic length scale over which the APD can respond to spatial variations in DI, while the $w(da/dx)$ term is an adjustment due to the breaking of $\pm x$ symmetry caused by the directionality and finite speed of wave propagation.

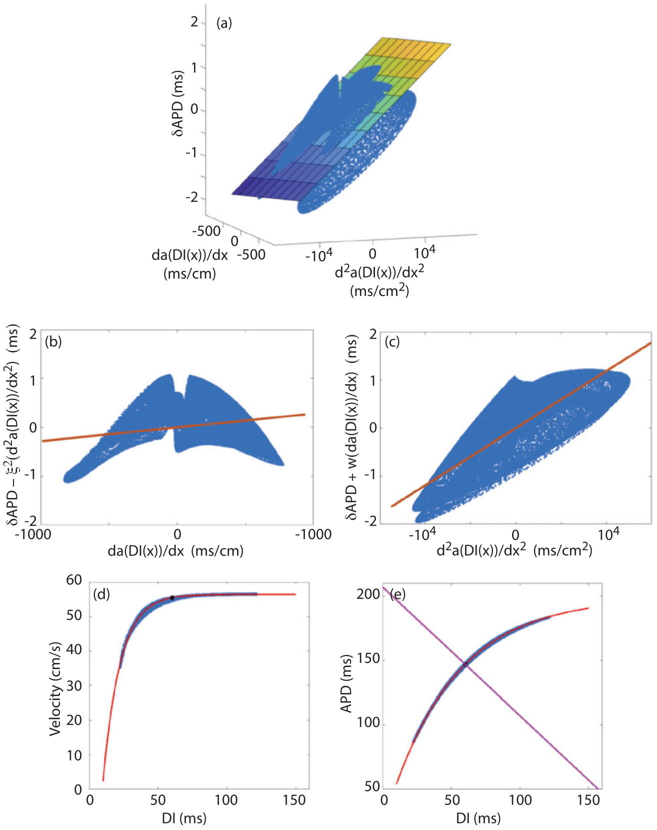

FIG. 7. Spread of the simulation data about the presumed relationship expressed by Eq. (13), due to the APD's nonuniformity in x, for the EC2 system, with BCL = 207 ms. (a) Scatterplot of $\delta\text{APD} \equiv \text{APD}(x) - a(\text{DI}(x))$ vs $da(\text{DI}(x))/dx$ and $d^2a(\text{DI}(x))/dx^2$ (in turquoise blue). The plane shown is the least-squares fit to the scatterplot data, obtained using the method described in Appendix B 3. Also shown are the scatterplot data and least-squares fit from (a) plotted vs (b) $da(\text{DI}(x))/dx$ and (c) $d^2a(\text{DI}(x))/dx$, with dependence on the other derivative subtracted out. Also included are the scatterplots (in blue) of the (d) wave velocity and (e) APD, vs DI. Red curves are the fitted APD and velocity restitution functions.

We expect a relationship of this type to exist, because adjacent cells with different APDs must necessarily have different membrane potentials on the trailing edge of their respective action potentials. Gap-junction current would then tend to flow from cells with longer APDs to those with shorter APDs, which tends to shorten the former and lengthen the latter. The membrane potential is thus subject to a diffusion process, accounting for the second derivative appearing in Eq. (13). Additional details appear in [69].

We explored the hypothesized relationship given by Eq. (13) by creating scatterplots of $\delta\text{APD}(x)$, defined to be $\text{APD}(x) - a(\text{DI}(x))$, vs $d(a(\text{DI}))/dx$ and $d^2(a(\text{DI}))/dx^2$, using simulation data. The results are shown in Figs. 7(a)–7(c). We can think of $\delta\text{APD}(x)$ as representing the departure of measured APDs from the values we would have obtained in the absence of spatial variations of the preceding $\text{DI}(x)$ and neighboring APDs. We then fitted a plane to the data, as shown in Fig. 7(a). To define the plane, we used the Newton-Raphson method to solve a multiple nonlinear regression problem in which the five parameters were β_1, β_2, β_3, w, and ξ^2. We assumed the APD had the functional form defined by Eq. (13), where $a(\mathrm{DI})$ is in the form

$$a(\mathrm{DI}) = \beta_1 - \beta_2 \exp(-\mathrm{DI}/\beta_3). \tag{14}$$

Scatterplot data used in the regression were obtained from a simulation for a given cycle length, excluding data close to the ends of the fiber and data from the first several waves of the simulation. Additional details about the method appears in Appendix B 3.

From Fig. 7(c) we see that the assumption of a linear relationship between $\delta\mathrm{APD}$ and $d^2(a(\mathrm{DI}))/dx^2$ is a good one; a strong linear relationship is seen to exist. On the other hand, we found that the linear contribution of the first derivative is actually small compared to its dependence on the square of $d(a(\mathrm{DI}))/dx$, as suggested by the parabolic shape of the spread of points in Fig. 7(b). This is due in part to the large amplitude of the alternans pattern, as suggested by the spread of data along the fitted APD and conduction velocity restitution functions [Figs. 7(d) and 7(e)]. However, we also found that, even when the cycle length is close to the bifurcation point (BCL = 215 ms) and the alternans amplitude is relatively small, the square term is still comparable to the linear term. At any rate, the spread of data seen in Fig. 7(b) is seen to be largely unaccounted for by the least-squares fit, with the opposite being true in Fig. 7(c), suggesting that ξ is the relevant length scale for describing the departure of the APD due to its dependence on x.

We calculated ξ for several different cycle lengths for all three of our three cases (GJ, EC1, and EC2), with the results shown in Fig. 6(d). We see that the relative sizes of ξ are roughly proportional to the nodal widths (i.e., the width of the transition region between domains) shown in Fig. 6(e). This suggests that the comparatively narrow nodal widths we observe for the EC1 and EC2 systems, compared to the GJ system, may be related to the characteristic diffusion lengths ξ.

Our calculation of the simulation values of ξ allowed us to compare the domain sizes from our simulations with theoretical predictions based on the work of Echebarria and Karma [69]. The latter predicts the domain size to be $(2\pi/\sqrt{3})(2\xi^2\Lambda)^{1/3}$, where $\Lambda = c^2(\mathrm{DI})/(2c'(\mathrm{DI}))$ and $c(\mathrm{DI})$ is the conduction velocity restitution relationship. We found that simulations and theoretical predictions agree surprisingly well, as can be seen by comparing Figs. 6(b) and 6(c), given that the theory is linear, whereas virtually all our simulations are in the nonlinear regime, with respect to both alternans amplitude and distance from the bifurcation point. In particular, we have seen that, even for low-amplitude alternans, quadratic terms in the alternans amplitude are apparently important, as suggested by Fig. 7(b). Critically, both simulations and theory predict that domain size is at least twofold to threefold larger in the GJ system, compared with EC1 and EC2.

As a final demonstration that the ability of the APD and membrane potential to vary over very short distances is a fundamental property of the EC1 and EC2 systems, in contrast to the GJ system, we performed a simple numerical experiment. We started all three systems with the same initial conditions

$$h(x, t = 0) = \begin{cases} 0.55 & \text{if } x \leqslant 1.6 \text{ cm} \\ 0.50 & \text{if } x > 1.6 \text{ cm}, \end{cases} \tag{15}$$

$$f(x, t = 0) = \begin{cases} 0.82 & \text{if } x \leqslant 1.6 \text{ cm} \\ 0.80 & \text{if } x > 1.6 \text{ cm}. \end{cases} \tag{16}$$

Thus, the left half of each system was initialized with uniform gating variable values that were slightly different from the right half, with an abrupt transition between two halves, at $x = 1.6$ cm. The entire fiber was then activated simultaneously by raising the membrane potential V_m to 15 mV in all cells at once. The results are shown in Fig. 8. As shown in Figs. 8(a)–8(c), the end of the action potential was essentially constant in each half of each system, except in the vicinity of the boundary between the two halves. Zooming in on this transition, we see in Figs. 8(d)–8(f) that the membrane potential gradient is much sharper in the two ephaptic-coupled systems EC1 and EC2 [Figs. 8(e) and 8(f)] than in the GJ system [Fig. 8(d)].

IV. DISCUSSION

Discordant alternans is potentially an important contributing factor in the onset of dangerous rapid rhythms in the heart, such as ventricular tachycardia and ventricular fibrillation. Attempts to study discordant alternans using computer simulation have been hampered, however, by difficulties in matching key properties of discordant alternans in simulations to their experimental counterparts. Importantly, these difficulties appear to be rooted in a fundamental problem with our understanding of the theory of how discordant alternans arises in cardiac tissue. The most perplexing of these difficulties centers on the size of discordant alternans domains. While the relatively small domain size seen in experiments can be obtained in simulations using standard models of gap-junction coupling, the high gap-junction resistances needed to obtain such domain sizes also slows down the wave conduction velocities to values well below those seen in experiments. Thus, to state the difficulties succinctly, using a standard tissue model that only incorporates cell-cell coupling through gap junctions, it is difficult to simulate realistic action potential wave speeds and small discordant alternans domain sizes under the same conditions.

To resolve this problem, we hypothesized that, when discordant alternans is present, both ephaptic and gap-junction coupling participate in the mechanism by which action potential wavefronts travel from one cell to the next. Further, we posited that, in contrast to the coupling mechanism involved on the wavefront, the coupling on the trailing edge of the wave (i.e., waveback) is dictated solely by gap-junction coupling. In this scenario, wavefront and waveback dynamics no longer depend on the same coupling mechanism. We suggest that this makes possible the simultaneous presence of rapid wave propagation speeds and small discordant alternans domain sizes, since the former is determined by wavefront dynamics, while the latter is governed by APD spatial coupling, in which waveback dynamics clearly plays a key role. We have found (Fig. 4), as others have [33,43,48,51,55], that ephaptic coupling on the wavefront can indeed produce rapid wave speeds for conditions with high gap-junction resistances that

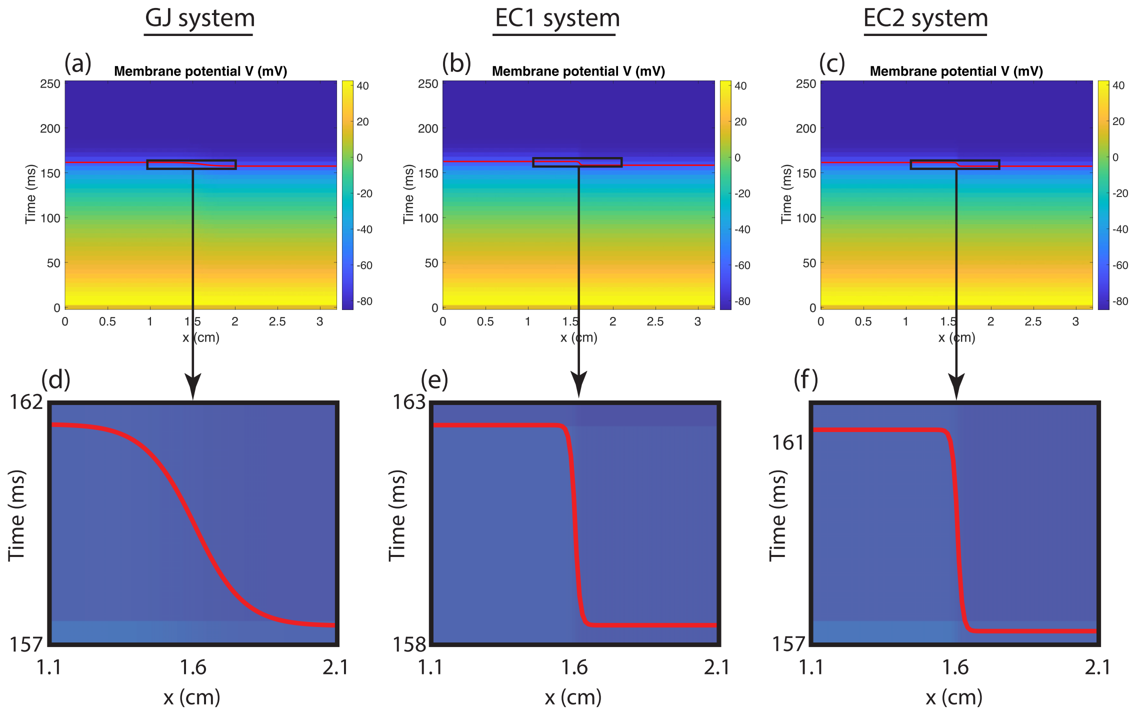

FIG. 8. Plots of V_m of a single action potential excited simultaneously at all points on the fiber at time $t = 0$, but with slightly different initial conditions in each half of the fiber: $h = 0.55$ and $f = 0.82$ for $x \leqslant 1.6$ cm, and $h = 0.50$ and $f = 0.80$ for $x > 1.6$ cm, for (a) the GJ system, (b) the EC1 system, and (c) the EC2 system. (d)–(f) Close-up of the location of the waveback (in red) for the conditions in (a)–(c) near the center of the fiber.

are consistent with the range of resistances measured experimentally [21–31]. Thus, we expected that, while ephaptic coupling mediated the fast velocity of the wavefront, low gap-junction conductivity would simultaneously decrease intercell coupling on the waveback, allowing APD to vary over short length scales, making small discordant alternans domain size possible.

To test these ideas, we first simulated tissue with comparatively low gap-junction resistance so that gap-junction coupling would dominate the dynamics on both the wavefront and waveback (the GJ system), to establish a baseline scenario. The result was wave propagation at physiologically realistic speeds (56.7 cm/s), but nonphysiologically large discordant alternans domains appeared [about 2.5 cm, as shown in Figs. 2(a) and 6(b)]. We then incorporated two changes motivated by experimental measurements and observations of gap-junction and sodium channel properties in myocytes [21–31,55,60]: We increased the gap-junction resistances by a factor of 100 and we redistributed most of the sodium channels (the fast-inward current) to the ends of the cells. These changes supported the ephaptic-coupling mechanism on the wavefront (but not on the waveback), as Fig. 3 shows. We found the wave speed to be nearly the same as the GJ system (approximately 57 cm/s), but the spatial patterning of discordant alternans was drastically different. Following transients from the initial conditions, incorporating these ephaptic-coupling effects resulted in discordant alternans domain sizes on the order of 1 cm in length, and sometimes substantially less than 1 cm in the EC2 system, for the shorter pacing cycle lengths [Fig. 6(b)]. Thus, incorporating ephaptic-coupling results in the domain sizes typically 3 times, and sometimes as much as 8 times, smaller than those seen in gap-junction-only coupling.

Even when the ephaptic-coupled systems tended towards producing larger domains (although still small compared to the gap-junction-dominated cases), as we saw in some of the EC1 simulations, we still found that the transition region between domains was much sharper than in the GJ system, again suggesting that the APD spatial coupling is much weaker in ephaptic-coupled systems. To provide further evidence for this, we directly tested the two ephaptic-coupling systems EC1 and EC2 to see if they could support sharp transitions in APD, by triggering an action potential simultaneously across the entire tissue with initial conditions that would lead to a sharp, abrupt spatial transition in APD if the cells were not coupled. Compared to the GJ system, the EC1 and EC2 systems exhibited transitions in APD that were much sharper and were confined to a spatial region ten times smaller than the transition region produced in the GJ system (Fig. 8).

While this study predicts that ephaptic coupling is necessary to support both fast wave propagation and steep repolarization gradients, this more broadly provides further support that ephaptic coupling is an important and critical mechanism of coupling under normal conditions. Importantly, we note that while our EC1 and EC2 systems included gap-junction resistances 100-fold higher than the GJ system, all the resistance values considered in this study (3.95–395 MΩ) are within the range of experimental measurements [21–31]. Specifically, in the scenarios in this paper, gap-junction resistance does not need to be low (e.g., 395 kΩ) to allow propagation speeds comparable to those seen in experiments (50–60 cm/s), consistent with measurements of gap-junction resistances that are much higher (3.95–395 MΩ). Other studies [33,43,47,51,55] have also demonstrated that low gap-junction resistance is not necessary for rapid (approximately 50 cm/s) action potential wave propagation. This leaves open two possibilities. (i) If gap-junction resistance is normally low, then it may be that wave propagation occurs through gap-junction connectivity, but ephaptic coupling may be responsible for rapid wave propagation in pathological remodeling in which gap-junction resistance is high. (ii) Alternatively, if gap-junction resistance is normally high, then it may be the case that rapid wave propagation is always mediated by both ephaptic and gap-junction coupling, with gap-junction coupling playing a supportive but still essential role. While other ionic, cellular, and tissue properties not considered in our modeling approach may also be important, our study provides strong evidence for ephaptic coupling as an important and necessary factor in the regulation of cardiac conduction.

We note that our study is not without limitations. In particular, our simulations use a minimal model of ion channel kinetics, which enabled the investigation of a wide range of parameters for cycle length, cleft width, gap-junction resistance, and fast-inward current conductance. Such a large parameter study would be highly computationally expensive using a more detailed biophysical model, due to the small numerical integration time step required for the subcellular discretization used in the tissue model. However, the key role of ephaptic coupling in this study is the support of a mechanism underlying wavefront and waveback independence and this manifests because of the biphasic or inverted U-shaped curve in the CV vs cleft width relationship (Fig. 4). Importantly, such a relationship has been previously shown by us [43,52] and others [33,42,54] for more detailed sodium current models, including Hodgkin-Huxley and Markov chain-based models, suggesting that the minimal model is appropriate for such investigation. Further, robust presentation of alternans spatial patterns in the minimal model [58,59] suggests it is ideal for our current study. Nonetheless, future work is needed to investigate alternans spatial patterns in additional ionic models and conditions.

ACKNOWLEDGMENTS

We gratefully acknowledge the National Science Foundation's Research Experience for Undergraduates Program, Grant No. DMS-1950189 (N.F.O. and L.M.), (including Darren Narayan), which supported two students (J.G. and M.H.), and the NSF Louis Stokes Alliance for Minority Participation Program and the RIT Ronald E. McNair Post-Baccalaureate Achievement Program (including Kate Torrey and JoVonna Victor), which jointly supported one undergraduate student (E.F.). This project was conceived at the Kavli Institute for Theoretical Physics, at the Integrative Cardiac Dynamics Workshop (N.F.O., A.K., S.H.W., L.M., and F.H.F.), via NSF Grant No. PHY-1748958. This study was supported by funding from National Institutes of Health Grants No. R01HL138003 (S.H.W.), No. R15HL147348 (N.F.O. and F.H.F.), and No. R01HL143450 (F.H.F.).

APPENDIX A: FINITE-DIFFERENCE SCHEME OF KIRCHOFF'S CURRENT LAW

The nodal voltages on each node of our system circuit were updated using a combination of the forward and backward Euler methods. Taking the node in the cleft region as an example (i.e., the node in the center of Fig. 1), we wrote Kirchhoff's current law (that is, the sum of currents leaving a node is zero) as

$$\begin{aligned} &-I_{\mathrm{cl}}(u_l, h_l, f_l) - I_{\mathrm{cl}}(u_r, h_r, f_r) \\ &+ C_{\mathrm{cl}}\frac{d(V_{\mathrm{cl}} - V_l)}{dt} + C_{\mathrm{cl}}\frac{d(V_{\mathrm{cl}} - V_r)}{dt} + \frac{V_{\mathrm{cl}}}{R_r} = 0, \end{aligned}$$

where V_{cl} is the cleft nodal voltage, V_l and V_r are the nodal voltages on the nodes closest to the cleft in the cells to the left and right, and u_l, h_l, f_l and u_r, h_r, f_r are the dynamical variables associated with the ion currents flowing into the cleft node from the cells on the left and right, respectively. We then applied a finite-difference scheme to the equation above as

$$\begin{aligned} &-I_{\mathrm{cl}}\big(u_l^n, h_l^n, f_l^n\big) - I_{\mathrm{cl}}^n\big(u_r^n, h_r^n, f_r^n\big) \\ &+ C_{\mathrm{cl}}\frac{V_{\mathrm{cl}}^{n+1} - V_l^{n+1} - V_{\mathrm{cl}}^n + V_l^n}{\Delta t} \\ &+ C_{\mathrm{cl}}\frac{V_{\mathrm{cl}}^{n+1} - V_r^{n+1} - V_{\mathrm{cl}}^n + V_r^n}{\Delta t} + \frac{V_{\mathrm{cl}}^{n+1}}{R_r} = 0, \end{aligned}$$

where the superscripts n and $n+1$ refer to the values at the nth and $(n+1)$st time steps, respectively. Finite-difference schemes at other nodes were applied to the equations at other nodes in the same manner, with the nodal voltages associated with the resistors evaluated at the future time step $n+1$, while the dynamical variables u, h, and f associated with the ion channel currents were evaluated at the current time step n. Use of future rather than present voltages on the resistors allowed us to take much larger time steps, since the fastest timescales were associated with voltage diffusion through the resistive components of the system.

To advance these equations from one time step to the next, that is, from time step n to time step $n+1$, we wrote the collection of all terms evaluated at the future $[(n+1)\mathrm{st}]$ time step as a sparse matrix A multiplied onto a vector $\mathbf{x}$ of all the dynamical variables evaluated at this future time step. The resulting vector was set equal to the vector containing all the remaining terms $\mathbf{b}$ (i.e., the terms evaluated at the present time step n). This matrix equation $A * \mathbf{x} = \mathbf{b}$ was then solved using MATLAB's `mldivide` method, written in the code as `x = A \ b`.

To facilitate construction of the matrices and vectors in this formulation, we used an object-oriented approach, in which components (i.e., the resistors, capacitors, and nonlinear current elements) were added to the matrix A and vector $\mathbf{b}$ one at a time, which we found to be much simpler than adding the Kirchhoff current law equation for each node to A and $\mathbf{b}$ one at a time. However, the two approaches are equivalent and result in the same set of equations.

APPENDIX B: CALCULATION OF CHARACTERISTIC DISCORDANT ALTERNANS DOMAIN PARAMETERS

1. Number and size of discordant alternans domains

The number of discordant alternans domains was calculated by taking the average over 200 waves of the number of rotations the point $(\mathrm{APD}(x), (d\mathrm{APD}/dx)(x))$ made around the point $(\langle\mathrm{APD}\rangle, \langle d\mathrm{APD}/dx\rangle)$ in $(\mathrm{APD}, d\mathrm{APD}/dx)$ space and then multiplying by 2. Data close to either end of the fiber were not used, to avoid effects from the boundaries. These 200 waves were taken from near the end of the simulation (e.g., waves 477–676 out of a simulation containing 726 waves, when $\mathrm{BCL} = 207$ ms). Specifically, for each of these 200 waves, we calculated

$$\theta_j = \tan^{-1}\frac{\mathrm{APD}(x_j) - \langle\mathrm{APD}\rangle}{(d\mathrm{APD}/dx)(x_j) - \langle d\mathrm{APD}/dx\rangle}, \tag{B1}$$

$$\Delta\theta_j = \theta_j - \theta_{j-1}, \tag{B2}$$

$$N_{\mathrm{domains}} = \frac{1}{\pi}\sum_{j=20}^{N_x-20}\Delta\theta_j, \tag{B3}$$

$$l_{\mathrm{domain}} = (N_x - 39)\Delta x/N_{\mathrm{domains}}, \tag{B4}$$

where $\langle\mathrm{APD}\rangle$ and $\langle d\mathrm{APD}/dx\rangle$ are the means of APD_j and $(d\mathrm{APD}/dx)_j$ over the grid points used, $20 \leqslant j \leqslant N_x - 20$, where $N_x = 320$; $x_j = (j-1)\Delta x$ is the coordinate of grid point j; and $\tan^{-1}$ evaluates to the angle consistent with a smoothly increasing winding number (i.e., no jumps). Here N_{domains} and l_{domain} were used to plot the number of discordant alternans domains and their average length, respectively, vs cycle length, in Figs. 6(a) and 6(b).

2. Domain node width

As is clear from Fig. 2, the width of the transition region between domains varies considerably across the different systems we studied. To form a quantitative measure of the width of this transition region, we first found the maximum and minimum APDs in each wave and divided the difference of these APDs by the largest APD gradient in that wave. Data within 20 grid points of each end of the fiber were excluded when determining these minimum and maximum quantities. We then averaged this quantity over all the waves to obtain our measure of the transition region typical for this system and pacing interval, which we called the nodal width. Specifically, we defined the nodal width to be

$$l_{\mathrm{node}} = \frac{1}{N_{\mathrm{waves}}}\sum_{n=1}^{N_{\mathrm{waves}}}\frac{\max_j(\mathrm{APD}_j) - \min_j(\mathrm{APD}_j)}{\max_j\,(|(d\mathrm{APD}/dx)_j|)}.$$

Here the number of waves N_{waves} excluded the first 50 and last 50 waves in the simulation, for a total of 627 waves when the BCL was 207 ms. Figure 6(e) shows l_{node} vs BCL for the three systems, GJ, EC1, and EC2.

3. Calculation of ξ and w

To calculate ξ and w, we assume, as Echebarria and Karma did [69], that the $\mathrm{APD}(x)$ at a given location x is its value $a(\mathrm{DI}(x))$ given by the restitution function $a(\mathrm{DI})$ plus a correction due to variations in APD in neighboring cells, which falls off with distance. Thus, we assume

$$\mathrm{APD}(x) = \int_{-\infty}^{\infty} a(\mathrm{DI}(x-\eta))G(\eta)d\eta,$$

where $G(\eta)$, defined so that $\int G(\eta)d\eta = 1$, is a function that describes the interaction of the APDs as a function of distance η. Expanding $a(\mathrm{DI}(x-\eta))$ as a Taylor series in η around x, we see that

$$\mathrm{APD}(x) \approx a(\mathrm{DI}(x)) - \frac{d}{dx}[a(\mathrm{DI}(x))]\int \eta G(\eta)d\eta + \frac{1}{2}\frac{d^2}{dx^2}[a(\mathrm{DI}(x))]\int \eta^2 G(\eta)d\eta.$$

Identifying

$$w = \int \eta G(\eta)d\eta,$$

$$\xi^2 = \frac{1}{2}\int \eta^2 G(\eta)d\eta,$$

we obtain Eq. (13). Note that ξ is a measure of the width of $G(\eta)$ and thus is a measure of the characteristic length scale over which APD coupling takes place, while w is a measure of the $\pm\eta$ asymmetry of $G(\eta)$. Now, assuming that $a(\mathrm{DI})$ has a standard exponential shape

$$a(\mathrm{DI}) = \beta_1 - \beta_2\exp(-\mathrm{DI}/\beta_3),$$

we find we can write Eq. (13) as

$$\mathrm{APD} = \beta_1 - \beta_2 e^{\gamma\mathrm{DI}}[1 + \gamma\mathrm{DI}'\tilde{w} + \gamma^2(\mathrm{DI}')^2\xi^2 + \gamma\mathrm{DI}''\xi^2], \tag{B5}$$

where $\gamma = -1/\beta_3$, $\tilde{w} = -w$, and DI' and DI'' are the first and second derivatives of DI, respectively, with respect to x. Using simulation data for APD, DI, DI', and DI'', we first conducted nonlinear multiple regression on Eq. (B5) with $\xi^2 = 0$ and $\tilde{w} = 0$, yielding preliminary values for β_1, β_2, and γ, the parameters for $a(\mathrm{DI})$. We then used the Newton-Raphson method to solve the full regression problem, using as the initial guess these three parameters, together with $\tilde{w} = 0$ and $\xi^2 = 0$. Convergence to the values for all five parameters β_1, β_2, γ, $\tilde{w}$, and ξ^2, which provided the least-squares fit, was usually obtained with only three iterations. The final values of β_1, β_2, and γ were always very close to those used in the initial guess for the full problem. The remaining parameters could then be immediately calculated: $w = -\tilde{w}$ and $\beta_3 = -1/\gamma$.

---

[1] J. M. Pastore, S. D. Girouard, K. R. Laurita, F. G. Akar, and D. S. Rosenbaum, Circulation **99**, 1385 (1999).

[2] M. A. Watanabe, F. H. Fenton, S. J. Evans, H. M. Hastings, and A. Karma, J. Cardiovasc. Electrophysiol. **12**, 196 (2001).

[3] Z. Qu, A. Garfinkel, P.-S. Chen, and J. N. Weiss, Circulation **102**, 1664 (2000).

[4] J. J. Fox, M. L. Riccio, F. Hua, E. Bodenschatz, and R. F. Gilmour, Jr., Circ. Res. **90**, 289 (2002).

[5] B.-R. Choi, W. Jang, and G. Salama, Heart Rhythm **4**, 1057 (2007).

[6] A. Gizzi, E. Cherry, R. F. Gilmour, Jr., S. Luther, S. Filippi, and F. H. Fenton, Front. Physiol. **4**, 71 (2013).

[7] M. R. Guevara, G. Ward, A. Shrier, and L. Glass, IEEE Comput. Cardiol. **562**, 167 (1984).

[8] J. Nolasco and R. W. Dahlen, J. Appl. Physiol. **25**, 191 (1968).

[9] E. M. Cherry and F. H. Fenton, Am. J. Physiol. **286**, H2332 (2004).

[10] D. Sato, Y. Shiferaw, A. Garfinkel, J. N. Weiss, Z. Qu, and A. Karma, Circ. Res. **99**, 520 (2006).

[11] D. Sato, D. M. Bers, and Y. Shiferaw, PLoS One **8**, e85365 (2013).

[12] C. Huang, Z. Song, J. Landaw, and Z. Qu, Biophys. J. **118**, 2574 (2020).

[13] H. Hayashi, Y. Shiferaw, D. Sato, M. Nihei, S.-F. Lin, P.-S. Chen, A. Garfinkel, J. N. Weiss, and Z. Qu, Biophys. J. **92**, 448 (2007).

[14] S. Mironov, J. Jalife, and E. G. Tolkacheva, Circulation **118**, 17 (2008).

[15] C. De Diego, R. K. Pai, A. S. Dave, A. Lynch, M. Thu, F. Chen, L.-H. Xie, J. N. Weiss, and M. Valderrábano, Am. J. Physiol. **294**, H1417 (2008).

[16] Y.-C. Hsieh, J.-C. Lin, C.-Y. Hung, C.-H. Li, S.-F. Lin, H.-I. Yeh, J.-L. Huang, C.-P. Lo, K. Haugan, B. D. Larsen *et al.*, Heart Rhythm **13**, 251 (2016).

[17] I. Uzelac, Y. C. Ji, D. Hornung, J. Schröder-Scheteling, S. Luther, R. A. Gray, E. M. Cherry, and F. H. Fenton, Front. Physiol. **8**, 819 (2017).

[18] K. Kulkarni, R. Visweswaran, X. Zhao, and E. G. Tolkacheva, Biomed Res. Int. **2015**, 170768 (2015).

[19] I. Uzelac, A. Kaboudian, S. Iravanian, J. G. Siles-Paredes, J. C. Gumbart, H. Ashikaga, N. Bhatia, R. F. Gilmour, Jr., E. M. Cherry, and F. H. Fenton, Heart Rhythm O^2 **2**, 394 (2021).

[20] D. J. Christini, M. L. Riccio, C. A. Culianu, J. J. Fox, A. Karma, and R. F. Gilmour, Jr., Phys. Rev. Lett. **96**, 104101 (2006).

[21] T. Desplantez, E. Dupont, N. J. Severs, and R. Weingart, J. Membr. Biol. **218**, 13 (2007).

[22] B. R. Kwak and H. J. Jongsma, Mol. Cell. Biochem. **157**, 93 (1996).

[23] M. L. McCain, T. Desplantez, N. A. Geisse, B. Rothen-Rutishauser, H. Oberer, K. K. Parker, and A. G. Kleber, Am. J. Physiol. **302**, H443 (2012).

[24] A. Moreno, M. Rook, G. Fishman, and D. Spray, Biophys. J. **67**, 113 (1994).

[25] V. Valiunas, E. C. Beyer, and P. R. Brink, Circ. Res. **91**, 104 (2002).

[26] S. Verheule, M. J. A. van Kempen, P. H. J. A. te Welscher, B. R. Kwak, and H. J. Jongsma, Circ. Res. **80**, 673 (1997).

[27] R. White, J. Doeller, V. Verselis, and B. Wittenberg, J. Gen. Physiol. **95**, 1061 (1990).

[28] M. S. Nielsen, L. Nygaard Axelsen, P. L. Sorgen, V. Verma, M. Delmar, and N.-H. Holstein-Rathlou, Compr. Physiol. **2**, 1981 (2012).

[29] A. Rüdisüli and R. Weingart, Pflügers Arch. **415**, 12 (1989).

[30] R. Weingart, J. Physiol. **370**, 267 (1986).

[31] B. A. Wittenberg, R. White, R. D. Ginzberg, and D. C. Spray, Circ. Res. **59**, 143 (1986).

[32] R. S. Kieval, J. F. Spear, and E. Moore, Circ. Res. **71**, 127 (1992).

[33] J. P. Kucera, S. Rohr, and Y. Rudy, Circ. Res. **91**, 1176 (2002).

[34] R. M. Shaw and Y. Rudy, Circ. Res. **81**, 727 (1997).

[35] M. S. Spach, J. F. Heidlage, P. C. Dolber, and R. C. Barr, Circ. Res. **86**, 302 (2000).

[36] Y. Wang and Y. Rudy, Am. J. Physiol. **278**, H1019 (2000).

[37] Y. Xie, D. Sato, A. Garfinkel, Z. Qu, and J. N. Weiss, Biophys. J. **99**, 1408 (2010).

[38] B. Muller-Borer, D. Erdman, and J. Buchanan, IEEE Trans. Biomed. Eng. **41**, 445 (1994).

[39] Y. Xie, A. Garfinkel, P. Camelliti, P. Kohl, J. N. Weiss, and Z. Qu, Heart Rhythm **6**, 1641 (2009).

[40] K. J. Sampson and C. S. Henriquez, Am. J. Physiol. **289**, H350 (2005).

[41] Niels F. Otani, Eileen Figueroa, James Garrison, Michelle Hewson, Laura Muñoz, Flavio H. Fenton, Alain Karma, and Seth H. Weinberg, Phys. Rev. Lett. **130**, 218401 (2023).

[42] N. Wei, Y. Mori, and E. G. Tolkacheva, J. Theor. Biol. **397**, 103 (2016).

[43] S. Weinberg, Chaos **27**, 093908 (2017).

[44] M. B. Nowak, A. Greer-Short, X. Wan, X. Wu, I. Deschênes, S. H. Weinberg, and S. Poelzing, Biophys. J. **118**, 2829 (2020).

[45] M. B. Nowak, R. Veeraraghavan, S. Poelzing, and S. H. Weinberg, Front. Physiol. **12**, 731025 (2021).

[46] M. B. Nowak, S. Poelzing, and S. H. Weinberg, J. Mol. Cell. Cardiol. **153**, 60 (2021).

[47] J. Lin and J. P. Keener, Proc. Natl. Acad. Sci. USA **107**, 20935 (2010).

[48] J. Lin and J. P. Keener, IEEE Trans. Biomed. Eng. **60**, 576 (2013).

[49] J. Lin and J. P. Keener, Biophys. J. **106**, 925 (2014).

[50] N. Moise, H. Struckman, C. Dagher, R. Veeraraghavan, and S. Weinberg, J. Gen. Physiol. **153**, e202112897 (2021).

[51] Y. Mori, G. I. Fishman, and C. S. Peskin, Proc. Natl. Acad. Sci. USA **105**, 6463 (2008).

[52] A. Greer-Short, S. A. George, S. Poelzing, and S. H. Weinberg, Circ.: Arrhythmia Elec. **10**, e004400 (2017).

[53] E. Ivanovic and J. P. Kucera, J. Physiol. **599**, 4779 (2021).

[54] E. Hichri, H. Abriel, and J. P. Kucera, J. Physiol. **596**, 563 (2018).

[55] R. Veeraraghavan, J. Lin, G. S. Hoeker, J. P. Keener, R. G. Gourdie, and S. Poelzing, Pflügers Arch.: Eur. J. Physiol. **467**, 2093 (2015).

[56] K. Y. Joseph, J. A. Liang, S. H. Weinberg, and N. A. Trayanova, J. Mol. Cell. Cardiol. **162**, 97 (2022).

[57] B. Echebarria and A. Karma, Eur. Phys. J. Spec. Top. **146**, 217 (2007).

[58] S. Dai and D. G. Schaeffer, Chaos **20**, 023131 (2010).

[59] J. G. Restrepo and A. Karma, Phys. Rev. E **79**, 030906(R) (2009).

[60] R. Veeraraghavan and R. G. Gourdie, Mol. Biol. Cell **27**, 3583 (2016).

[61] E. Agullo-Pascual, X. Lin, A. Leo-Macias, M. Zhang, F.-X. Liang, Z. Li, A. Pfenniger, I. Lübkemeier, S. Keegan, D. Fenyö *et al.*, Cardiovasc. Res. **104**, 371 (2014).

[62] A. Leo-Macias, E. Agullo-Pascual, J. L. Sanchez-Alonso, S.

Keegan, X. Lin, T. Arcos, Y. E. Korchev, J. Gorelik, D. Fenyö, E. Rothenberg *et al.*, Nat. Commun. **7**, 10919 (2016).

[63] R. Veeraraghavan, J. Lin, J. P. Keener, R. Gourdie, and S. Poelzing, Pflügers Arch.: Eur. J. Physiol. **468**, 1651 (2016).

[64] M. Hong, L. Bao, E. Kefaloyianni, E. Agullo-Pascual, H. Chkourko, M. Foster, E. Taskin, M. Zhandre, D. A. Reid, E. Rothenberg *et al.*, J. Biol. Chem. **287**, 41258 (2012).

[65] M. L. Milstein, H. Musa, D. P. Balbuena, J. M. Anumonwo, D. S. Auerbach, P. B. Furspan, L. Hou, B. Hu, S. M. Schumacher, R. Vaidyanathan *et al.*, Proc. Natl. Acad. Sci. USA **109**, E2134 (2012).

[66] S. H. Vermij, H. Abriel, and T. A. van Veen, Cardiovasc. Res. **113**, cvw259 (2017).

[67] M. A. De Smet, A. Lissoni, T. Nezlobinsky, N. Wang, E. Dries, M. Pérez-Hernández, X. Lin, M. Amoni, T. Vervliet, K. Witschas *et al.*, J. Clin. Invest. **131**, e137752 (2021).

[68] X. Lin, N. Liu, J. Lu, J. Zhang, J. M. Anumonwo, L. L. Isom, G. I. Fishman, and M. Delmar, Heart Rhythm **8**, 1923 (2011).

[69] B. Echebarria and A. Karma, Phys. Rev. E **76**, 051911 (2007).